

# COMPARISON OF DEM AND TRADITIONAL MODELING METHODS FOR SIMULATING STEADY-STATE WHEEL-TERRAIN INTERACTION FOR SMALL VEHICLES

William Smith<sup>a</sup>, Daniel Melanz<sup>b</sup>, Carmine Senatore<sup>c</sup>, Karl Iagnemma<sup>c</sup>, and Huei Peng<sup>a</sup>

<sup>a</sup>Department of Mechanical Engineering, University of Michigan, 2350 Hayward Street, Ann Arbor, MI 48103

<sup>b</sup>Department of Mechanical Engineering, University of Wisconsin, 1513 University Avenue, Madison, WI 53706

<sup>c</sup>Laboratory for Manufacturing and Productivity, Massachusetts Institute of Technology, 77 Massachusetts Avenue, Cambridge, MA 02139  
[wsmithw@umich.edu](mailto:wsmithw@umich.edu), [melanz@wisc.edu](mailto:melanz@wisc.edu), [senator@mit.edu](mailto:senator@mit.edu), [kdi@mit.edu](mailto:kdi@mit.edu), [hpeng@umich.edu](mailto:hpeng@umich.edu)

---

## Abstract

A simulation study was conducted to evaluate three terramechanics methods used for predicting single wheel performance of small vehicles on granular terrain. Traditional Bekker-type terramechanics methods do not consider the soil profile, the soil dynamics, or the transient wheel dynamics, which can be important factors in vehicle performance. The ‘dynamic Bekker’ method used to overcome these limitations treats the wheel a free body, which allows for multibody dynamics simulations, and discretizes the soil into grid regions, which allows for more complex soil profiles. Another option is to use the discrete element method, which makes fewer assumptions but requires significantly more computation time. Before these methods can be evaluated in dynamic conditions, they must first be tested in steady-state operation. Single-wheel experiments were performed on Mojave Martian Simulant to evaluate performance at various slip ratios. Similar tests were simulated using three terramechanics methods: traditional Bekker, dynamic Bekker, and the discrete element method. Each method was tuned to match direct shear and pressure-sinkage tests performed on the same soil. While Bekker-type methods only require curve-fitting to determine soil parameters, the discrete element method was tuned by simulating the soil tests with varying parameters. The results from this study will help determine the accuracy of each method during steady-state, and whether the computation cost of the discrete element method is warranted for steady-state conditions.

**Keywords:** discrete element method, terramechanics, small vehicles

---

## 1 Introduction

Small autonomous and unmanned ground vehicles continue to increase in importance for many industries, from planetary exploration to military defense. Examples include the highly visible NASA rovers Spirit and Opportunity, and the iRobot PackBot. These vehicles require significantly fewer resources compared to manned vehicles while reducing risks to human life. The use of unmanned vehicles, including small vehicles, is likely to increase as advances are made in autonomy technologies. Given the critical nature of the tasks these vehicles are given, it is crucial they maintain their mobility.

Terramechanics methods can aid in the design and operation of small vehicles to help ensure they do not become immobilized due to limited traction or energy depletion. The most common terramechanics method is the Bekker method, discussed in greater detail in Section 2.1. This method, the product of many researches over decades, provides a steady-state relationship for wheel performance given the soil properties and wheel operating

condition. During off-road locomotion the vehicle’s dynamics couples with an irregular soil profile, can generate more complex wheel-soil interactions than assumed in the Bekker method. Two additional methods are also commonly used: the dynamic Bekker method and the discrete element method (DEM). These methods, described in detail in the following sections, allow for multibody dynamics simulations on complex soil profiles.

Each terramechanics method has advantages and disadvantages; no method is ideal for all situations. It is important then to determine when a given method should be chosen, and understand its limitations compared to other methods. In this paper three common terramechanics methods, the Bekker method, dynamic Bekker method, and DEM, are evaluated by comparing the predicted performance of a small wheel driving on Mojave Martian Simulant at steady state. The parameter values needed for each method were obtained by performing direct shear and pressure-sinkage soil tests. Evaluations were made based on quantitative and qualitative accuracy, and computation efficiency.

## 2 Terramechanics Methods

The three terramechanics methods, the Bekker method, dynamic Bekker method, and the discrete element method, are each described in the following sections.

### 2.1 Bekker Method

The limitations and difficulties of purely empirical or theoretical terramechanics methods led researchers to create semi-empirical models. M.G. Bekker, a pioneer in the field during the 1950s and 1960s, created semi-empirical equations for wheel performance which are the basis for most terramechanics models today [1] [2] [3]. The Bekker method, which encompasses all terramechanics methods derived from Bekker's original equations, is regularly used in its original or modified form. Recent examples include modification for wheel grousers [4] [5] [6] [7] and identifying soil properties during vehicle operation [8] [9].

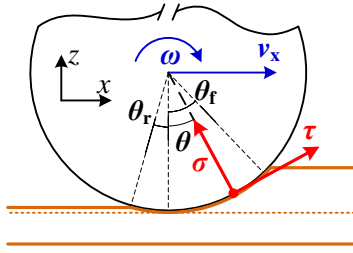


**Fig. 1.** Bekker method diagram of a driven rigid wheel on soft soil (modified from [10]).

The Bekker method simplifies the interaction between wheel and soil into a two dimensional representation where the wheel is a smooth circle traversing a flat, level soil, shown in Fig. 1. Since the soil is assumed to be significantly softer than the wheel, and to further simplify the model, the wheel is treated as a rigid body. The wheel sinks into the soil, as a combination of normal forces acting on the wheel and wheel slip ratio  $s$ , creating an interface from the entry contact angle  $\theta_f$  to the exit contact angle  $\theta_r$ . Wheel slip ratio, which depends on the angular velocity  $\omega$ , the linear velocity  $v_x$ , and the wheel radius  $r$ , is defined by

$$s = (\omega r - v_x) / v_x \quad (1)$$

Along the wheel-soil interface normal stresses  $\sigma$  and tangential stresses  $\tau$  develop, which can be integrated to find the forces acting on the wheel. The normal force, drawbar force (sum of thrust and resistance forces), and driving torque are defined by

$$F_{\text{normal}} = rb \int_{\theta_r}^{\theta_f} (\sigma \cos \theta + \tau \sin \theta) d\theta \quad (2)$$

$$F_{\text{drawbar}} = rb \int_{\theta_r}^{\theta_f} (\tau \cos \theta - \sigma \sin \theta) d\theta \quad (3)$$

$$T_{\text{wheel}} = r^2 b \int_{\theta_r}^{\theta_f} \tau d\theta \quad (4)$$

where  $b$  is the wheel width.

Normal stress along the interface is assumed to be equivalent to the normal pressure on a flat plate at the same sinkage  $z$ , the amount of vertical soil compression. The function for normal stress is defined by

$$\sigma = k \left( \frac{z}{b_{\text{plate}}} \right)^n \quad (5)$$

where  $k$  and  $n$  are pressure-sinkage parameters, which can be determined through plate-sinkage experiments, and  $b_{\text{plate}}$  is the width of the flat plate. The equation for sinkage has been modified somewhat to account for the bow-like shape of normal stress that occurs along the wheel-soil interface [11]. Sinkage along the interface is split between the front and rear regions, defined by

$$z = \begin{cases} r(\cos \theta - \cos \theta_f) & \theta_m \leq \theta \leq \theta_f \\ r(\cos \theta_{\text{eq}} - \cos \theta_f) & \theta_r \leq \theta < \theta_m \end{cases} \quad (6)$$

where the location of maximum stress  $\theta_m$  and the equivalent front-region contact angle  $\theta_{\text{eq}}$  equal

$$\theta_m = (a_0 + a_1 s) \theta_f \quad (7)$$

$$\theta_{\text{eq}} = \theta_f - (\theta_f - \theta_m) \frac{\theta - \theta_r}{\theta_m - \theta_r} \quad (8)$$

The coefficients  $a_0$  and  $a_1$  are used to empirically adjust the location of maximum stress according to wheel slip  $s$  and entry contact angle. These coefficients can only be determined through wheel tests. The rear contact angle  $\theta_r$  was assumed to equal zero in this study, which is a common assumption, especially for low cohesion soils.

Shear stress along the interface is determined by the semi-empirical equation

$$\tau_{s \geq 0} = \tau_{\text{res}} \left( 1 - \exp \left( \frac{-|j|}{K} \right) \right)$$

$$\tau_{s < 0} = \begin{cases} -\tau_{\text{res}} \left( 1 - \exp \left( \frac{-|j|}{K} \right) \right) & \theta \geq \theta_m \\ \tau_{\text{res}} \left( 1 - \exp \left( \frac{-|j|}{K} \right) \right) & \theta < \theta_m \end{cases} \quad (9)$$

where  $j$  is the shear displacement and  $K$  is the shear modulus coefficient [11] [12]. The residual shear stress  $\tau_{\text{res}}$  is determined according to the Mohr-Coulomb failure criteria, defined by

$$\tau_{\text{res}} = c + \sigma \tan \phi \quad (10)$$

where  $c$  is the soil cohesion and  $\phi$  is the angle of internal friction, both of which can be determined through soil tests. The shear displacement equation varies based on

the slip ratio and the location along the interface [11] [12], given by

$$j_{s>0} = r[(\theta_f - \theta) - (1-s)(\sin \theta_f - \sin \theta)]$$

$$j_{s<0} = \begin{cases} r(1-s) \left[ \frac{(\theta_f - \theta) \frac{\sin \theta_f - \theta_m}{\theta_f - \theta_m}}{-\sin \theta_f + \sin \theta} \right] & \theta \geq \theta_m \\ r[\theta_m - \theta - (1-s)(\sin \theta_m - \sin \theta)] & \theta < \theta_m \end{cases} \quad (11)$$

The Bekker method has several advantages compared to other terramechanics methods, including computation speed. While researchers have shown techniques to increase computation speed [13] [5], even its original form is computationally efficient compared to other techniques. Many of the soil coefficients can be determined through simple soil tests, as will be shown later in the paper. Other parameters, such as those used to determine  $\theta_m$ , can easily be determined if wheel test data is available.

The simplicity of the Bekker method, one of its primary advantages, creates several limitations. Modeling three-dimensional wheel-soil interaction, or a more complex tread pattern, for example, require significant modification to the Bekker method. Modifications to the Bekker method, which can improve numerical accuracy, often result in an increased number of empirical terms. Two examples include a more complex equation for  $n$  [14], and a modified normal pressure equation [15]. One of the most significant limitations is that the Bekker method describes steady-state relationships, not dynamic equations. This restriction limits its applicability for transient operation, such as multibody vehicle simulations.

## 2.2 Dynamic Bekker Method

The dynamic Bekker method addresses two of the limitations of the Bekker method: the ability to simulate multibody dynamics and complex soil profiles. While several variations of the dynamic Bekker method have been presented, similar to the Bekker method the fundamental concept is the same. The dynamic Bekker method treats the wheel as a free body with inertia, and discretizes the soil so the Bekker stress equations can be applied to each region. Researchers have used variations of the dynamic Bekker method to perform multibody simulations with [16] [17], and without [18] [19] [5] soil discretization. The following is a description of the dynamic Bekker method used in this paper.

The model is composed of two major elements: a single rigid body representing the wheel and multiple rigid bodies representing the soil, shown in Fig. 2. The wheel is bilaterally constrained to move at a specified linear and angular velocity to produce a desired slip ratio. The Lagrange multipliers that are produced by the solution of this constrained multibody dynamics problem provide the drawbar pull and driving torque required to propel the wheel. A vertical force is applied at the wheel hub to

produce the desired normal load.

The soil is represented by a uniformly spaced set of spheres, or soil nodes, supported by nonlinear springs constrained to move only in the vertical direction. As the soil nodes come into contact with the wheel body, the nodes will be displaced. This displacement, or sinkage, is used in Eq. (5) to determine the resulting soil normal pressure. The pressure is multiplied by the area that the soil node acts on the wheel, which is the distance between the centers of the adjacent soil nodes multiplied by the wheel width. The normal force acts on the wheel in the plane of wheel-node contact. Using the normal pressure Eq. (9) is used to calculate the shear force, which is applied in the tangential plane of wheel-node contact.

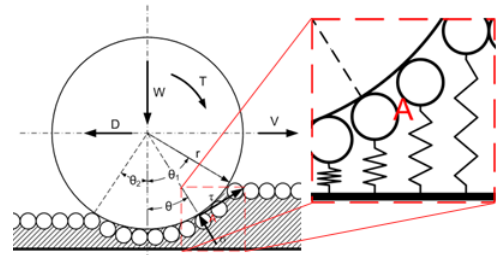


**Fig. 2.** Diagram of the dynamic Bekker model. The close-up region A shows the how the wheel contacts the soil nodes.

The tool used to create this model, called Chrono, has been built to leverage parallel computing and specializes in simulations involving large amounts of contact and friction. Chrono is both modular and extensible, stemming from the desire to build vertical applications such as this terramechanics module.

## 2.3 Discrete Element Method

Numerical methods such as the discrete element method (DEM) have been used for terramechanics since the 1970s and continue to increase in popularity as computing resources improve [20]. The discrete element method (DEM) represents soil as a collection of many discrete elements, where each element is defined by its size, shape, position, velocity, and orientation. When particles collide, either with another particle or with a wall, forces and torques are generated using explicit equations. By modeling soil using individual particles, DEM allows for significant soil deformation and transport, and the modification of properties such as soil packing structure and non-homogeneity. Recently examples of the use of DEM include the modeling of complex soil interactions during wheel-digging and blade-cutting of soil [21] [22].

The software used in this study was a modified form of LIGGGHTS, a version of the open-source software LAMMPS developed at the Sandia National Laboratories [23].

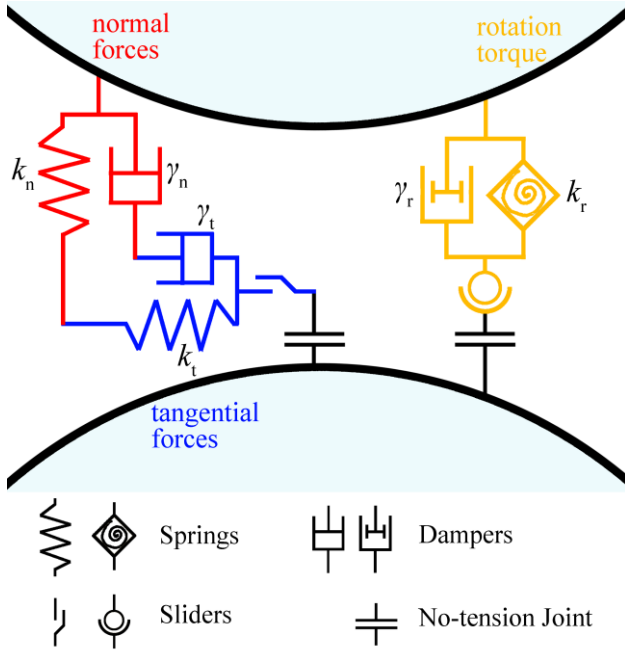


**Fig. 3.** DEM contact model for particle-particle force/torque interactions (after [24]).

In this study all particles are spherical with normal and tangential Hertzian style friction forces  $\mathbf{F}_{n/t}$  [25] [26] [27] [28] and rolling friction moment  $\mathbf{T}_r$ , shown in Fig. 3. When particles collide, the reaction force is determined by the length and velocity of particle-particle overlap. Forces normal to the contact plane (along the unit vector between particles) are described by

$$\mathbf{F}_n = k_n \delta \mathbf{n}_{ij} - \gamma_n \mathbf{v}_n \quad (12)$$

where  $\delta$  is the overlap length of the two particles,  $\mathbf{n}_{ij}$  is the unit vector connecting the centers of each particle, and  $\mathbf{v}_{n/t}$  is the normal component of the relative velocity of the two particles. The normal elastic spring coefficient  $k_n$  and viscoelastic damping coefficient  $\gamma_n$  are defined by

$$k_n = \frac{4}{3} Y_{\text{eff}} \sqrt{\frac{R_i R_j}{R_i + R_j}} \delta \quad (13)$$

$$\gamma_n = -2 \sqrt{\frac{5}{6}} \beta \sqrt{1.5 k_n \frac{M_i M_j}{M_i + M_j}}$$

where  $R_{ij}$  and  $M_{ij}$  are the radius and mass of each particle, respectively. The effective Young's modulus  $Y_{\text{eff}}$  and the coefficient  $\beta$  are defined by

$$Y_{\text{eff}} = \frac{Y_i Y_j}{Y_i (1 - \nu_j^2) + Y_j (1 - \nu_i^2)} \quad (14)$$

$$\beta = \frac{\ln(e)}{\sqrt{\ln^2(e) + \pi^2}}$$

where  $Y_{ij}$  is the Young's modulus of each particle,  $\nu_{ij}$  is the Poisson ratio of each particle, and  $e$  is the coefficient of restitution.

Similarly, forces tangential to the contact plane are

described by

$$\mathbf{F}_t = k_t \Delta \mathbf{s}_t - \gamma_t \mathbf{v}_t \quad (15)$$

where  $\Delta \mathbf{s}_t$  is the tangential displacement vector between the two particles for their entire contact duration and  $\mathbf{v}_t$  is the tangential component of the relative velocity of the two particles. The tangential elastic spring coefficient  $k_t$  and viscoelastic damping coefficient  $\gamma_t$  are defined by

$$k_t = 8 G_{\text{eff}} \sqrt{\frac{R_i R_j}{R_i + R_j}} \delta \quad (16)$$

$$\gamma_t = -2 \sqrt{\frac{5}{6}} \beta \sqrt{k_t \frac{M_i M_j}{M_i + M_j}}$$

where  $G_{\text{eff}}$  is the effective shear modulus, defined by

$$G_{\text{eff}} = \frac{0.5 Y_i Y_j}{Y_i (2 + \nu_j) (1 - \nu_j) + Y_j (2 + \nu_i) (1 - \nu_i)} \quad (17)$$

An upper limit exists for tangential forces through the Coulomb criterion given by

$$\text{if } |\mathbf{F}_t| > \mu_c |\mathbf{F}_n| \text{ then } |\mathbf{F}_t| = \mu_c |\mathbf{F}_n| \quad (18)$$

where  $\mu_c$  is the static yield coefficient.

Real soil grains have considerable angularity, causing them to interlock and inhibiting rotation. Many researchers have shown that when only using normal and tangential friction forces, more realistic particle shapes such as ellipsoids, poly-ellipsoids, polyhedrals, and complex shapes formed through the clumping of spheres, can better reproduce soil behavior compared to spheres [29] [30] [21]. The disadvantage of using complex shapes include increased computation time and increased program complexity. Using a rolling resistance term has been shown to provide similar results to complex particle shapes but without a significant penalty in computation speed [31] [32] [33].

An elastic-plastic spring-dashpot (epsd) rolling resistance model was used in this study, which was shown to be a better model compared to constant directional torque and viscous models [34]. The rolling resistance model uses a spring and damper, similar to the friction forces. The torque contribution  $\mathbf{T}_r$  acts against relative angular motion between two contacting bodies, defined by

$$\mathbf{T}_r = \min \left( \mathbf{T}_r^k + \mathbf{T}_r^\gamma, \mu_{r, \text{eff}} \frac{R_i R_j}{R_i + R_j} \mathbf{F}_n \right) \quad (19)$$

where  $\mathbf{T}_r^{k/\gamma}$  are the stiffness/damping torque and  $\mu_{r, \text{eff}}$  is the effective rolling resistance coefficient. Torque is limited by the resistance coefficient and normal force similar to tangential friction. Rolling stiffness and damping terms depend on the relative rotation vector  $\Delta \boldsymbol{\theta}_r$  and the relative angular velocity vector  $\Delta \boldsymbol{\omega}_r$ , respectively, given by

$$\mathbf{T}_{r, t+\Delta t}^k = \mathbf{T}_{r, t}^k + \Delta \mathbf{T}_r^k \quad (20)$$

$$\mathbf{T}_r^\gamma = \gamma_r \Delta \boldsymbol{\omega}_r$$

$$\Delta \mathbf{T}_r^k = -k_r \Delta \boldsymbol{\theta}_r$$

The rolling elastic spring coefficient  $k_r$  and the rolling viscoelastic damping coefficient  $\gamma_r$  are defined by

$$k_r = 2.25k_n \left( \mu_{r, \text{eff}} \frac{R_i R_j}{R_i + R_j} \right)^2 \quad (21)$$

$$\gamma_r = 2\sqrt{k_r I_{\text{eff}}}$$

where  $I_{\text{eff}}$  is the effective moment of inertia of the particles in contact, defined by

$$I_{\text{eff}} = 1.4 \frac{M_i R_i^2 M_j R_j^2}{M_i R_i^2 + M_j R_j^2} \quad (22)$$

Recent research on granular soils, particularly soils with angular particles, has found that particle interaction forces are velocity dependent. Soil simulant SSC-2, a silty sand with fine angular grains originally intended as an analogue for Martian regolith, exhibits an increasing drag force when velocity increased from 1 to 50 mm/s [35]. In granular pile formation DEM simulations, the rolling friction coefficient was found to be dependent on the relative motion between particles [32]. In this study the effective rolling resistance coefficient is dependent on the square of the relative velocity between particles, defined by

$$\mu_{r, \text{eff}} = \min(\mu_r |\mathbf{v}_t|^2, 1.0) \quad (23)$$

where  $\mu_r$  is the user-specified rolling resistance. This modification to the standard epsd rolling resistance model was necessary to accurately model the slow shear rate for direct-shear tests and the high sinkage rate for pressure-sinkage tests, using the same set of DEM parameters.

The complexity of the discrete element method is responsible for many of the method's advantages and limitations. By modeling the soil using small discrete particles, DEM has the capability to analyze the micro and macro-properties of soil. Unlike finite element methods, can easily handle large soil deformation and fault cracks. DEM also does not require empirical equations to handle wheel simulations, and can be expanded without modification to model interaction with other objects, such as legs.

The additional complexity of DEM also limits its applicability. There lacks an efficient, robust method to determine the DEM parameter values necessary to produce the desired macro-mechanical properties. While computation power has greatly increased since DEM was first created, it is still necessary to model soils with significantly larger particles than in reality. Finally, DEM requires careful consideration of properties in addition to parameter values, such as particle packing structure and particle shape.

### 3 Soil Testing

Mojave Martian Simulant (MMS) [36] was used in all experiments for this paper. MMS was characterized by performing direct shear and pressure-sinkage tests. The results from each test were used to determine the parameter values for the three terramechanics methods.

Choosing parameter values to fit the soil tests, rather than the wheel tests, better evaluates the prediction accuracy of each simulation method.

### 3.1 Experimental Tests

Soil shear properties greatly influence wheel performance, especially through traction generation. Direct shear tests were used to measure the shear strength properties of MMS. The shear box was approximately 60 x 60 x 60 mm (W x L x H) in size. Three normal pressures (2080, 5330, 17830 Pa) were tested for loosely-packed soil with bulk density between 1.55 and 1.6 g/cm<sup>3</sup>. The lower half of the shear box moved approximately 6.5 mm in 6 minutes, creating a shear rate of 18.0  $\mu\text{m/s}$ . Two tests were performed at each normal load and averaged.

Soil normal properties also greatly influence wheel performance, especially through sinkage generation. Pressure-sinkage tests were performed using a 5 x 15 cm (W x L) in size for loosely-packed soil with bulk density between 1.55 and 1.6 g/cm<sup>3</sup>. The flat plate penetrated the soil at a rate of 10.0 mm/s to a depth of 2 cm. Fifteen tests were performed and averaged.

### 3.2 Bekker Parameter Identification

The experimental direct-shear results were used to determine the Bekker parameters  $c$ ,  $\phi$ , and  $K$  by numerically minimizing the error given by

$$\arg \min_{c, \phi, K} \sum \left[ \tau(j) - (c + \sigma \tan \phi) \left( 1 - \exp\left(\frac{-|j|}{K}\right) \right) \right]^2 \quad (24)$$

The resulting Bekker shear stress curves are shown in Fig. 4. Error minimization was performed using the data from all normal loads so that one set of parameters was obtained.

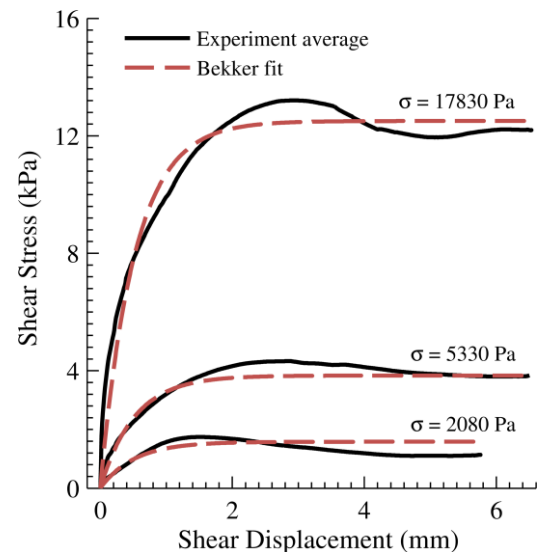
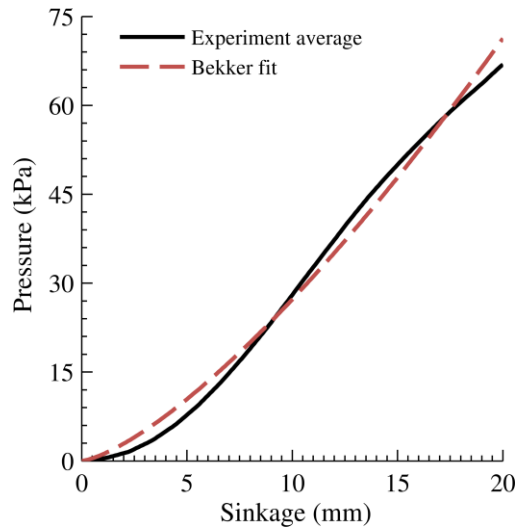


Fig. 4. Bekker parameter fit for direct shear tests.





**Fig. 5.** Bekker parameter fit for pressure sinkage tests.

**Table 1.** Bekker parameter values from direct-shear and pressure-sinkage curve fitting.

Parameter	Value
$c$ [Pa]	139.280
$\phi$ [rad]	0.606
$K$ [m]	$5.151 \times 10^{-4}$
$k$ [Pa]	$2.541 \times 10^5$
$n$ [-]	1.387

The experimental pressure-sinkage results were used to determine the Bekker parameters  $k$  and  $n$  by numerically minimizing the error given by

$$\arg \min_{k,n} \sum \left[ \sigma(z) - k \left( \frac{z}{b_{\text{plate}}} \right)^n \right]^2 \quad (25)$$

The resulting Bekker pressure curves are shown in Fig. 5. The final Bekker parameters for MMS obtained from both soil tests are shown in Table 1. These parameters are applicable for both the Bekker and dynamic Bekker methods. It is important to note that the pressure-sinkage parameters are sensitive to the plate size used, the maximum sinkage depth, and the penetration rate [37].

### 3.3 Discrete Element Method Tests

The parameter values for the discrete element method cannot be determined through curve fitting, as with the Bekker method, because the normal and shear properties cannot be described by the contact equations alone. Instead, DEM direct-shear and pressure-sinkage simulations similar to the real experiment must be performed.

The temporal increment, or time step, of DEM simulations must be small enough to preserve stability, yet

large enough to produce reasonable computation times. The maximum allowable time step is a function of  $(M_i/k_n)^{1/2}$  [38] [39] [22], placing a computation penalty on small soil particles and high Young's modulus values. After selecting an initial time step according to the function, simulations were performed at varying time step to ensure stability. In addition to the time step penalty, decreasing particle size results in an increased number of particles per unit volume, further reducing computation time. It was found that a wider range of particle values was beneficial to simulation accuracy, while particles too large in size decreased simulation repeatability. After evaluating numerous particle distribution ranges and shape functions, a linear distribution of 2.5 - 10 mm was chosen.

Soil particle arrangement, or packing, has a significant impact on macroscopic soil behavior [40]. The procedure used in this paper was to pour particles under Earth gravity into a 50 x 50 mm (W x L) rectangular prism to a height of 160 mm. After the particles settled, the soil particle density was modified to produce a bulk density of 1.6 g/cm<sup>3</sup>, roughly equal to the true value. Simulations with different time steps have slightly different particle density values due to the randomness that occurs with this method. Periodic boundaries in the  $x$  and  $y$  planes were used to allow the prism to be repeated in the  $xy$ -plane, building a larger soil body. This technique was used to create the soil bodies in the pressure-sinkage and wheel locomotion tests.

Significant research has already been performed in the area of DEM parameter selection and validation, using methods such as direct shear tests [41] [42], angle of repose tests [33] [43] [32], and triaxial compression tests [21] [29] [31] [44]. The techniques and insights from the literature provided a basis for parameter selection in this work, however given the number of DEM parameters, configurations, and settings, hundreds of soil test simulations were required to obtain reasonable accuracy. The soil parameters which were found to best reproduce the real soil behavior for both direct shear and pressure-sinkage tests are listed in Table 2. Mesh walls, used in direct shear and pressure-sinkage tests, were assumed to be smooth with zero friction and low restitution.

**Table 2.** DEM soil parameters and simulation settings.

Parameter	Value
particle diameter [mm]	2.5 - 10
particle density [g/cm <sup>3</sup> ]	3.072 - 3.107
bulk density [g/cm <sup>3</sup> ]	1.6
$Y$ [Pa]	$7.0 \times 10^7$
$\nu$ [-]	0.35
$\mu_c$ [-] (particle, wall)	0.86, 0.0
$\mu_r$ [-] (particle, wall)	$6.75 \times 10^8$ , 0.0
$e$ [-] (particle, wall)	0.4, 0.06

### 3.3.1 Direct Shear Test

Numerous DEM direct shear tests were simulated during the process of parameter selection. Tests were conducted by first generating an upper and lower shear box mesh using the real shear box dimensions. Particles were then poured into the shear box to a height of 60 mm, where particle density was chosen based on the previously described particle packing method. The desired normal load was then applied to the soil using a flat plane of tightly packed particles grouped into a rigid body. The particle densities were chosen to produce the desired normal force. The inertia of the body was not an issue due to the low shear rate. After the normal pressure stabilized, the upper box and rigid body were translated at a constant shear rate of  $6.6 \times 10^{-4}$  m/s for a distance of 6.6 mm. Shear stress was calculated by measuring the  $x$ -plane force of the upper mesh, and dividing by the original  $xy$ -plane area. The simulation test parameters are listed in Table 3.

**Table 3.** DEM direct shear test settings and parameters.

Parameter	Value
shear box dimensions [mm]	60 x 60 x 60 (W x L x H)
normal load [Pa]	2080, 5330, 17830
shear rate [mm/s]	0.66
shear displacement [mm]	6.6
number of soil particles	~640
time step [sec]	1.5 - $3.8 \times 10^{-6}$

While the experimental shear rate was considerably slower than the simulated rate, reducing the simulated shear rate had negligible impact on shear stress curves. An example simulation is displayed in Fig. 6 for a normal load of 17830 Pa. The figure shows the horizontal additions to the upper and lower meshes used to keep the particles within the bin.

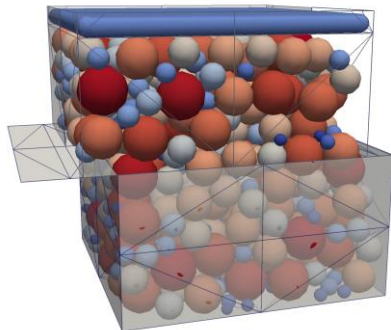


**Fig. 6.** DEM simulation of direct-shear test at normal load 17830 Pa (soil shading indicates radius).

Five direct shear tests were performed using the DEM parameter values given in Table 2 for time steps ranging from 1.5 to  $3.8 \mu\text{s}$ . The particle pouring method has an

element of randomness, which along with the relatively large particle sizes, contributes to variation among simulations. Simulation results, including the average and standard deviation shear stress, are shown in Fig. 7. The simulated residual shear stress is somewhat higher than experimental, however this was a compromise made to produce better pressure-sinkage results. Simulations were run on a single core of an Intel Xeon 5160 (3.0 GHz), at a rate of 40 to 20 cpu minutes per simulation second for time steps 1.5 and  $3.8 \mu\text{s}$ , respectively.

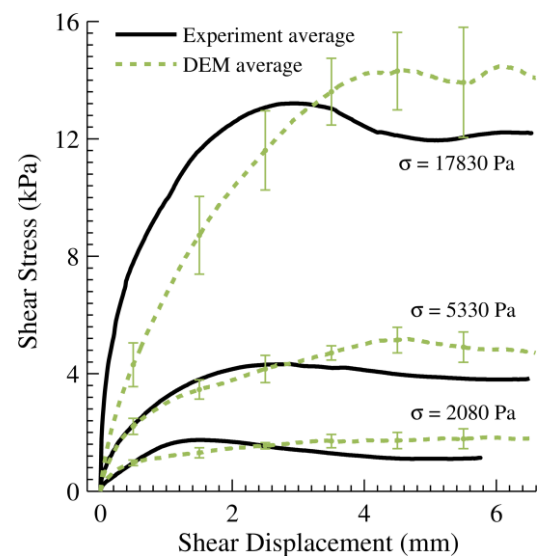


**Fig. 7.** DEM direct shear average results with standard deviation bars.

### 3.3.2 Pressure-Sinkage Test

Numerous pressure-sinkage tests were simulated during the process of parameter selection. Due to the large number of simulations required, it was important to reduce computation time where possible. Reduction in the number of soil particles was accomplished by simulating a soil bin approximately three times the size of the pressure plate. Periodic boundaries were used in the  $x$  and  $y$  dimensions to help remove wall effects, better representing a larger soil bin. Computation time was also reduced by using the previously generated soil prisms, described in Section 3.3, to build the soil body. This step eliminated the need to perform soil packing for a large volume. The pressure plate, generated as a mesh, was moved into the soil at a fixed sinkage rate of 10 mm/s. Normal pressure was determined by dividing the  $z$ -plane force acting on the mesh plate by the  $xy$ -area of the plate. The simulation test parameters are listed in Table 4, with an example simulation displayed in Fig. 8.

**Table 4.** DEM pressure-sinkage test settings and parameters.

Parameter	Value
soil bin dimensions [mm]	150 x 400 x 160 (W x L x H)
plate dimensions [mm]	50 x 130 x 10 (W x L x H)
sinkage rate [mm/s]	10.0
maximum sinkage [mm]	20.0
number of soil particles	~30,000
time step [sec]	1.5 - 3.8x10 <sup>-6</sup>

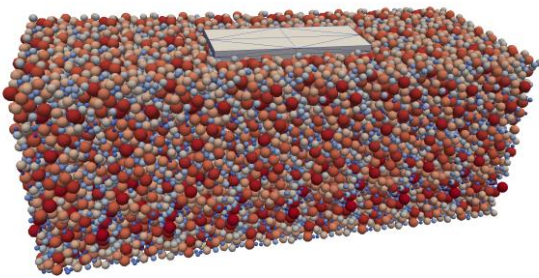


**Fig. 8.** DEM simulation of pressure-sinkage test (soil shading indicates radius).

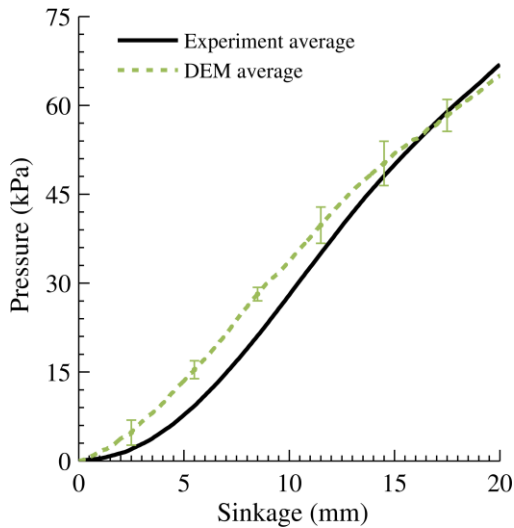


**Fig. 9.** DEM pressure sinkage average results with standard deviation bars.

Five pressure-sinkage tests were performed using the DEM parameter values given in Table 2 for time steps ranging from 1.5 to 3.8  $\mu$ s. Variation among simulations is again attributed to the randomness of the pouring method used for particle packing and the relatively large particle sizes. Simulation results, including the average and standard deviation normal pressure, are shown in Fig. 9. Simulated pressure is slightly higher than experimental for low sinkage values between 2.5 and 12.5 mm,

however this was a compromise made to produce better direct shear results. Simulations were run on a single core of an Intel Xeon 5160 (3.0 GHz), at a rate of 6 to 3 hours cpu per simulation second for time steps 1.5 and 3.8  $\mu$ s, respectively.

## 4 Wheel Testing

Steady-state, constant slip ratio wheel tests are the most common wheel performance test and method for evaluating terramechanics methods. A wheel is placed in the center of a rectangular soil bin, where the soil is flat and smooth. An additional mass or force is applied to the wheel to produce the desired normal load. After the wheel position stabilizes, an  $x$ -axis force and a  $y$ -axis torque are applied to the wheel to maintain the desired linear and angular velocities, respectively. Common wheel performance outputs from the test include drawbar pull (sum of forces in the  $x$ -axis), wheel driving torque, and sinkage. Tests were simulated using the three terramechanics methods and compared to experimental results.

### 4.1 Experimental Tests

Wheel test experiments were performed using the single wheel test bed located at the Massachusetts Institute of Technology [45]. The test bed, shown in Fig. 10, consists of a Lexan soil bin surrounded by an aluminum frame. A carriage slides on two rails, allowing for longitudinal ( $x$ -axis) motion of the wheel. The wheel can rotate in the  $y$ -axis while connected to a mount which translates in the vertical or  $z$ -axis. Longitudinal carriage motion is controlled by a toothed belt, while the wheel is directly driven by a DC motor. A 6-axis force torque transducer is mounted between the wheel mount and the carriage to measure drawbar pull and vertical force. A flange-to-flange reaction torque sensor is used to measure driving torque applied to the wheel. The soil used for the wheel tests was MMS, the same soil as used for direct shear and pressure-sinkage tests.

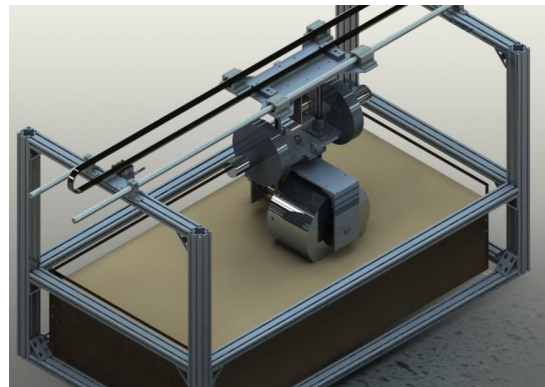


**Fig. 10.** Diagram of MIT wheel test bed.



The wheel used in this study had a width of 160 mm and a radius of 130 mm. The wheel surface did not contain lugs or grousers, but was coated with MMS using glue. This procedure made the shearing interaction along the wheel-soil interface better mimic the behavior of the direct shear tests, while providing a more realistic surface friction compared to smooth aluminum. An additional normal force was applied to the wheel to generate a normal load of 115 N. Experiments were conducted for 9 slip ratios with a constant angular velocity of 17 deg/s. Tests were run for a distance of 0.7 m, or until steady state was reached. The properties of the experimental wheel tests are detailed in Table 5. It should be noted that the method of determining wheel sinkage was by measuring the vertical position of the wheel mount over time. This method is not precise because it does not measure at the wheel-soil interface. If the soil varies in height over the length of the test bed, the sinkage measurement will be directly influenced.

**Table 5.** Experimental wheel test properties.

Parameter	Value
soil bed dimensions [mm]	600 x 1000 x 160 (W x L x H)
wheel width [mm]	160.0
wheel radius [mm]	130.0
wheel mass [kg]	3.2
normal load [N]	115.0
angular velocity [deg/s]	17.0
slip ratios [-]	-0.7, -0.5, -0.3, -0.1, 0.0, 0.1, 0.3, 0.5, 0.7

## 4.2 Simulation Settings

The following is a description of any additional parameters or settings required for wheel simulations of each terramechanics method.

### 4.2.1 Bekker Method

The majority of parameter values for the Bekker method were determined through parameter fitting of the direct shear and pressure-sinkage soil tests, listed in Table 1. Some of the parameters, such as  $a_0$  and  $a_1$  from Eq. (7) used to determine  $\theta_m$ , cannot be determined through these soil tests. These parameters can only be determined experimentally through wheel tests. The goal of this paper is to determine the accuracy of each terramechanics method's prediction, not fit, of wheel performance. Therefore, rather than use the experimental wheel results to determine these parameters, they were assumed using coefficients from the literature [46]. Similarly, the rear contact angle  $\theta_r$  was assumed equal to zero. These parameters are given in Table 6.

**Table 6.** Additional Bekker parameter values used for wheel simulations.

Parameter	Value
$a_0$ [-]	0.18
$a_1$ [-]	0.32
$\theta_r$ [rad]	0

The Bekker method is extremely efficient to solve, requiring about 43 ms to solve for a given slip ratio and normal load [10]. It should be noted that unlike the dynamic Bekker and discrete element methods, the Bekker method solves for a steady-state relationship as opposed to a dynamic time series.

### 4.2.2 Dynamic Bekker Method

The dynamic Bekker method used the same Bekker parameters listed in Table 1 and Table 6. The added capability of the dynamic method also adds complexity to its computation. Since the dynamic method computes a time series, there is a need to select a simulation time step. A convergence analysis was performed by evaluating the steady state wheel sinkage at varying time step values, shown in Fig. 11. A time step between  $1 \times 10^{-3}$  and  $1 \times 10^{-4}$  was found to obtain convergence. The figure also displays the computation cost of a reduction in time step.

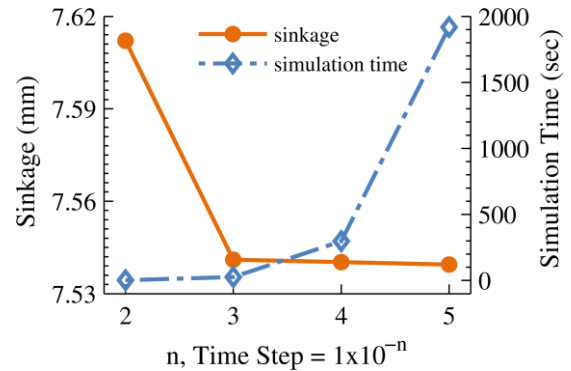


**Fig. 11.** Dynamic Bekker convergence analysis for simulation time step. Simulation time is the cpu time per one second of simulation.

The number of soil nodes, or node spacing, was also evaluated using a similar convergence analysis, shown in Fig. 12. Steady state wheel sinkage converges for 300 or more nodes, corresponding to a node spacing of 3.3 mm or less. The figure also shows the computation cost of increasing the number of nodes. This cost is a result of an increased number of bodies that must be examined during collision detection.

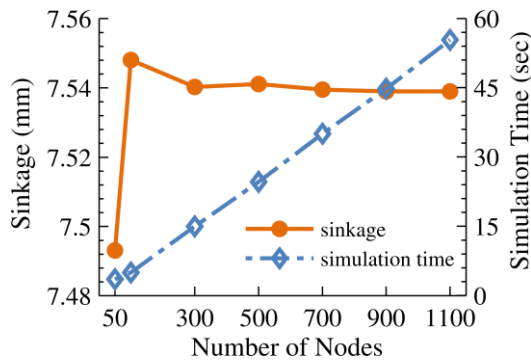


**Fig. 12.** Dynamic Bekker convergence analysis for number of nodes (node spacing). Simulation time is the cpu time per one second of simulation.

A rendering of the dynamic Bekker model, implemented in Chrono, is shown in Fig. 13. The computation times given in Fig. 11 and Fig. 12 correspond to the cpu seconds per simulation second on a single core of an AMD Opteron 6274 2.2GHz processor.

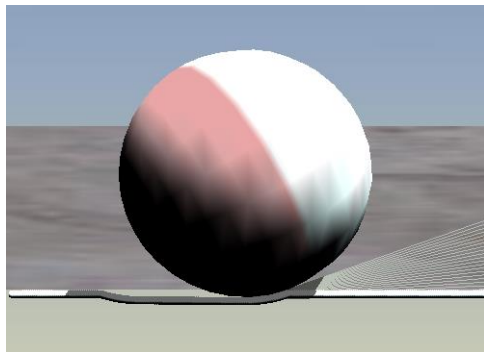


**Fig. 13.** A rendering of the dynamic Bekker model.

#### 4.2.3 Discrete Element Method

Wheel tests were simulated using the discrete element method using the parameters found by simulating the direct shear and pressure-sinkage soil tests, shown in Table 2. The DEM wheel consists of many 1 cm diameter particles that overlap to approximate a smooth surface. The typical distance between particles was 75 % of the particle radius. The wheel particles were grouped together to act as a single rigid body, similar to the flat plate used in direct shear simulations. The wheel was constrained so that it could only translate in the longitudinal and vertical directions and rotate in the y-axis, similar to the experimental conditions. A rendering of a DEM wheel simulation is shown in Fig. 14 for 50% slip ratio.

The soil bed had approximately the same dimensions as the experimental facility, requiring about 300,000 particles. The soil bed was constrained in the  $x$  and  $y$  dimensions by fixing the position of soil particles along the border, outside of the soil bed (not pictured in the

figure). At the beginning of the simulation, the wheel was placed at one end of the soil bed and given 0.5 seconds to rest. Afterwards a force in the  $x$ -direction and a  $y$ -axis torque were applied for 1 second to ramp-up the longitudinal and angular velocities to their desired value. The wheel was then simulated for a distance of 0.7 m, or until steady state was reached. At high slip ratios the longitudinal velocity is very low, and steady state is reached before 0.7 m.

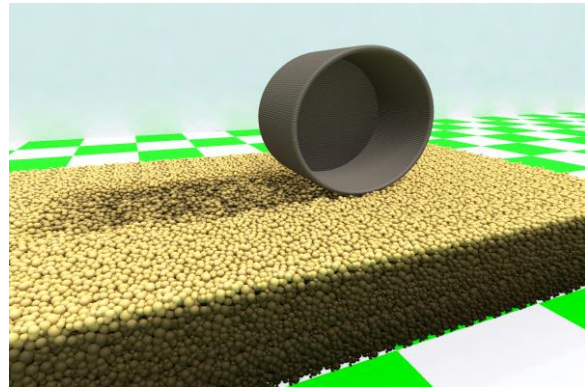


**Fig. 14.** DEM wheel simulation at 50% slip (soil shading indicates elevation).

**Table 7.** DEM wheel test settings and parameters.

Parameter	Value
soil bed dimensions [mm]	600 x 1000 x 160 (W x L x H)
number of soil particles	~300,000
number of wheel particles	~12,000
time step [sec]	$2.2 \times 10^{-6}$

Because the experimental wheel was covered with soil, the soil parameters were also used to describe the wheel-soil interaction. Simulations were run on 8 cores, using 4 Intel Xeon 5160 processors, on a single server blade. On average the computation rate was 8.5 hours of computation time per simulation second at a time step of  $2.2 \mu\text{s}$ . Given the time required to simulate each slip ratio (e.g. 166 hours per 19 second simulation, using 8 cores), only one time step was used.

#### 4.3 Simulation Results

Steady-state performance results were calculated by averaging the last several seconds of data, for both simulated and experimental results. Steady state results for drawbar pull, driving torque, and sinkage are compared in Fig. 15, Fig. 16, and Fig. 17, respectively. Results for drawbar pull and driving torque show similar trends. DEM provides the best fit of the experimental results, both quantitatively and qualitatively. The Bekker method has similar results as DEM for large positive and

negative slip ratios, but error is significantly larger near zero slip. The differences between the dynamic and original Bekker methods, which use essentially the same equations, can be attributed to implementation of the dynamic method and soil discretization.

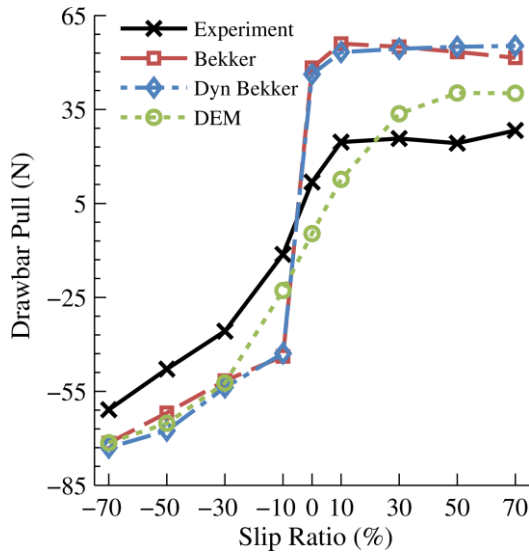


**Fig. 15.** Simulation drawbar pull at steady-state compared to experimental sinkage.

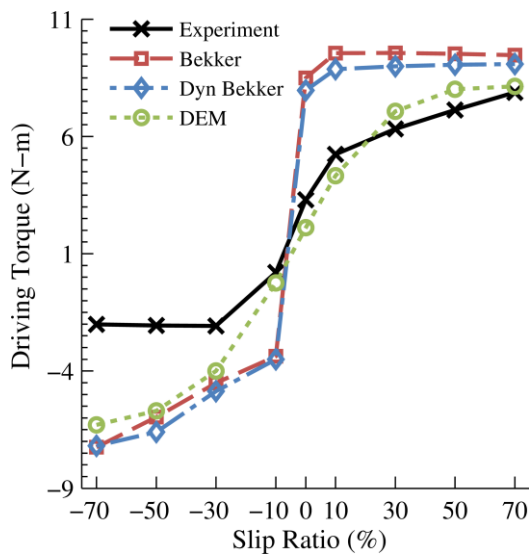


**Fig. 16.** Simulation driving torque at steady-state compared to experimental sinkage.

When examining the wheel sinkage results it is important to recall the measurement uncertainty inherent in the test rig. Standard deviation bars are shown for experimental results to better illustrate this uncertainty. Given the measurement uncertainty, it is still possible to compare the three terramechanics methods using overall trends. DEM has much better qualitative agreement to the experimental results, though the percent error of the Bekker methods can be smaller at certain slip ratios.

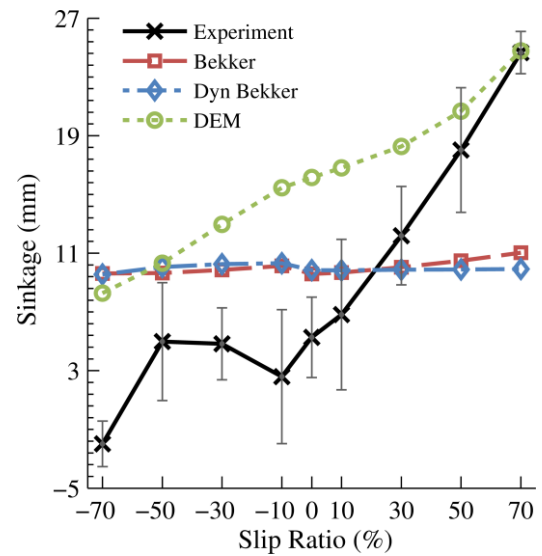


**Fig. 17.** Simulation sinkage at steady-state compared to experimental sinkage, with experimental standard deviation bars.

When considering the performance of the Bekker model the role of parameters  $K$ ,  $a_0$ , and  $a_1$ , should be further discussed. Shear modulus  $K$ , as measured in this paper, is extremely low when compared to values for similar soils found in the literature [46]. This discrepancy is not due to different intrinsic behavior of the material but it is a consequence on how the shear modulus is calculated [47]. Utilizing Wong's approach for calculating  $K$  would yield a larger value, which would improve Bekker model predictions at low slip. Moreover, it should be noted that parameters  $a_0$  and  $a_1$  are taken from literature and they may not be representative of the wheel-terrain configuration under investigation. Slip-sinkage behavior is sensitive to these parameters and better agreement between experimental data and Bekker model may be obtained if  $a_0$  and  $a_1$  were available. However, it should be noted that these parameters can only be calculated through wheel experiments and they cannot be derived from soil tests (e.g. bevameter).

The dynamic Bekker method and DEM can be compared using time-series data in addition to steady-state values. Four seconds of drawbar pull and driving torque time-series data is shown in Fig. 18 and Fig. 19, respectively. The experimental results show low frequency periodicity which reflects the periodic failure pattern within the soil. Other researchers have shown similar behavior for wheel tests on sandy terrain [48]. The dynamic Bekker method models the soil as essentially a nonlinear spring without damping, and as a result oscillates at a high frequency. DEM results have a lower frequency periodicity with higher amplitude compared to experimental data, which may be a result of the relatively large soil particles used.

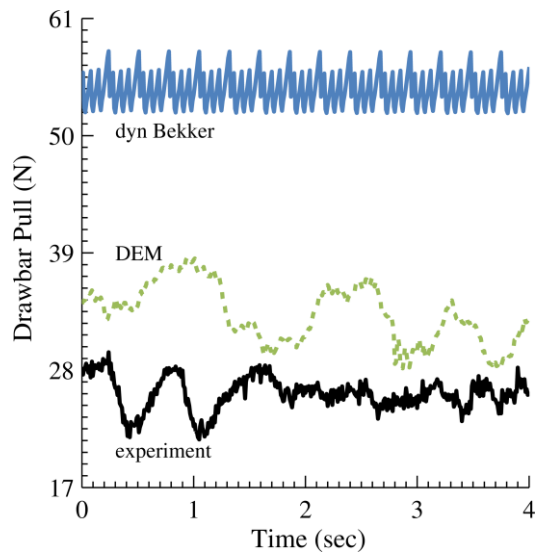


**Fig. 18.** Drawbar pull time series comparison of experiment and dynamic terramechanics models. Time shown is a random 4 seconds during steady-state operation.

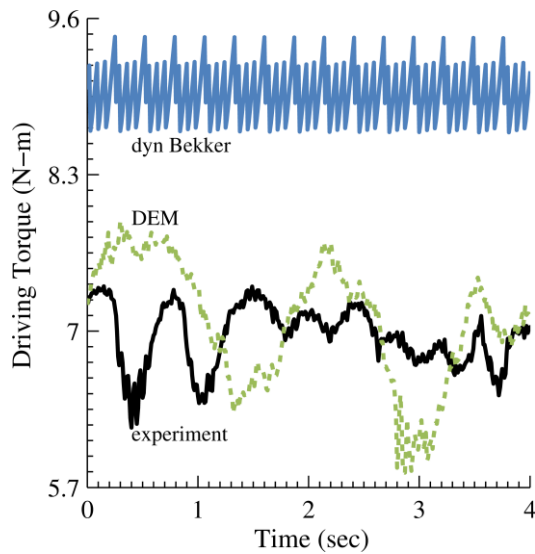


**Fig. 19.** Driving torque time series comparison of experiment and dynamic terramechanics models. Time shown is a random 4 seconds during steady-state operation.

## 5 Conclusions

Three common terramechanics modeling methods were evaluated by selecting parameter values from soil tests and comparing steady state wheel performance with experimental data. Time series experimental results were also compared to the two dynamic terramechanics methods. The results from this paper give better insight into the advantages and disadvantages of each method, while providing a direct comparison of prediction accuracy.

The Bekker method showed why it continues to be

used and developed by researchers. Parameter selection from both soil tests provided a simple, efficient method for parameter selection. With only a few additional parameters that could not be derived from the soil tests, the Bekker method generated wheel test results with reasonable qualitative agreement. If wheel data is available then many of the parameter values can be chosen to greatly reduce quantitative error. However if wheel data is already available then the need for a terramechanics model is greatly reduced.

The discrete element method produced more accurate wheel performance, both quantitatively and qualitatively, compared to both Bekker methods. This accuracy came with a large penalty in computation effort and efficiency. Significant time and effort was required to fit both direct shear and pressure-sinkage results using a single set of DEM parameters. Once parameter values were determined, each wheel simulation required several days to complete when using 8 computation cores. It should be noted that DEM has significantly greater simulation capabilities than either Bekker method. It is possible, for example, to model a more complex wheel shape digging into the soil [21]. In addition to average value steady-state agreement, DEM also showed similar time-series results. The periodic nature of the wheel-soil interaction can be useful in areas such as full vehicle multibody analysis and selection of electronic powertrain components. Further study is required to determine methods of improving the accuracy of the periodic signal.

Without wheel experimental data, it appears that Bekker methods are likely to produce significant errors, at least for small vehicles, due to their reliance on several empirical parameters. Given the computational limitations of DEM, it is desirable to use the Bekker method when possible. In situations where the capabilities of the Bekker method are sufficient, it may be possible to create a DEM simulation which could be used to tune the Bekker parameters. To better illustrate this point, and show the flexibility of the Bekker method, parameters were determined through combined least squares minimization of DEM drawbar, driving torque, and sinkage data (shown in Table 8).

**Table 8.** Bekker parameter values determined by fitting to DEM results.

Parameter	Value
$c$ [Pa]	96.240
$\phi$ [rad]	0.606
$K$ [m]	$4.534 \times 10^{-3}$
$k$ [Pa]	$2.305 \times 10^4$
$n$ [-]	0.418
$a_0$ [-]	0.09
$a_1$ [-]	0.90
$\theta_r$ [rad]	0



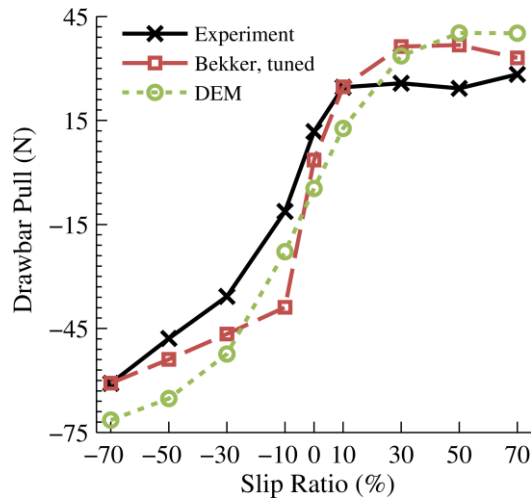


Fig. 20. Bekker fit of DEM drawbar pull.

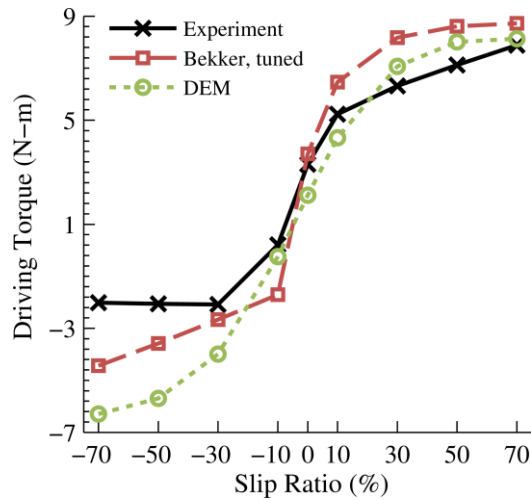


Fig. 21. Bekker fit of DEM driving torque.

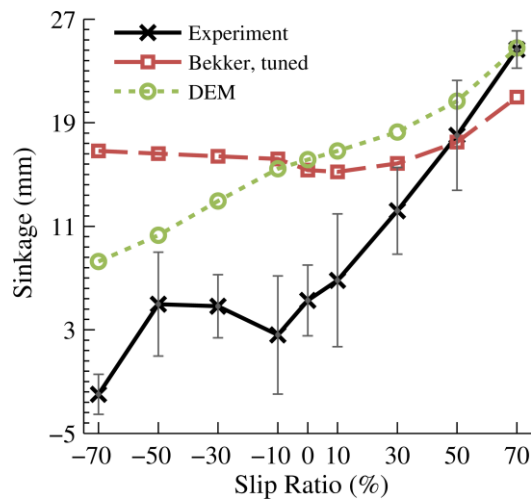


Fig. 22. Bekker fit of DEM sinkage.

The resulting drawbar, driving torque, and sinkage curves using the DEM-tuned Bekker parameters are shown in Fig. 20, Fig. 21, and Fig. 22, respectively. The figures show close agreement with the DEM results, thereby reducing the Bekker method error. Agreement is worse for negative slip values, especially regarding sinkage.

While the Bekker method can be tuned to match DEM results for single wheel locomotion on flat, level ground, it is still uncertain how well the dynamic Bekker method can model multibody vehicle simulations and rough terrain. Comparison of DEM and the dynamic Bekker method for these conditions remains an area of future study.

## Nomenclature

$\beta$	Coefficient used to relate damping ratio to collision time of particles	[-]
$\gamma_{n/t}$	Normal/tangential viscoelastic damping coefficient	[N-s/m]
$\gamma_r$	Rolling viscoelastic damping coefficient	[N-m/s]
$\Delta\theta_r$	Relative rotation vector	[rad]
$\Delta\omega_r$	Relative angular velocity vector	[rad/s]
$\Delta s_t$	Tangential displacement vector for the duration of particle contact	[m]
$\Delta T_r^k$	Change in rolling resistance stiffness torque	[N-m]
$\delta$	Overlap length of two particles	[m]
$\theta$	Angle along wheel-soil interface	[rad]
$\theta_{eq}$	Equivalent front-region contact angle for rear-region	[rad]
$\theta_{f/r}$	Wheel-soil entry/exit angle	[rad]
$\theta_m$	Position of maximum radius stress	[rad]
$\mu_c$	Coulomb static yield coefficient	[-]
$\mu_{r, eff}$	Effective rolling resistance coefficient	[-]
$\mu_r$	Rolling resistance coefficient	[-]
$\nu_{i/j}$	Poisson ratio of particle i/j	[-]
$\sigma$	Normal pressure	[N/m <sup>2</sup> ]
$\tau$	Shear stress	[N/m <sup>2</sup> ]
$\tau_{res}$	Mohr-Coulomb residual shear stress	[N/m <sup>2</sup> ]
$\phi$	Angle of internal friction	[rad]
$\omega$	Wheel angular velocity	[rad/s]
$a_{0,1}$	Bekker coefficients for $\theta_m$	[-]
$b$	Wheel width	[m]
$b_{plate}$	Plate width	[m]
$c$	Soil cohesion	[Pa]
$e$	Coefficient of restitution	[-]
$F_{n/t}$	Hertzian normal/tangential friction forces	[N]
$F_{normal}$	Normal force of wheel	[N]
$G_{eff}$	Effective shear modulus	[Pa]
$I_{eff}$	Effective moment of inertia	[kg-m <sup>2</sup> ]
$j$	Soil displacement due to shearing	[m]

$K$	Bekker shear modulus coefficient	[m]
$k$	Bekker pressure-sinkage parameter	[N/m <sup>2</sup> ]
$k_{n/t}$	Normal/tangential elastic spring coefficient	[N/m]
$k_r$	Rolling elastic spring coefficient	[N-m]
$M_{i/j}$	Mass of particle $i/j$	[kg]
$n$	Bekker pressure-sinkage exponent	[-]
$\mathbf{n}_{ij}$	Unit vector connecting the centers of two overlapping particles	[-]
$R_{i/j}$	Radius of particle $i/j$	[m]
$r$	Wheel radius	[m]
$s$	Slip ratio	[-]
$T_r$	Rolling resistance torque	[N-m]
$T_r^{k/\gamma}$	Rolling resistance stiffness/damping torques	[N-m]
$\mathbf{v}_{n/t}$	Normal/tangential component of the relative velocity of two particles	[m/s]
$v_x$	Wheel linear velocity in direction of travel	[m/s]
$v_j$	Shear displacement rate	[m/s]
$Y_{\text{eff}}$	Effective Young's modulus	[Pa]
$Y_{i/j}$	Young's modulus of particle $i/j$	[Pa]
$z$	Soil sinkage	[m]

## Acknowledgements

This work is supported in part by a Science, Mathematics & Research for Transformation (SMART) Scholarship. The authors of this paper would like to acknowledge members of the US Army Tank Automotive Research Development and Engineering Center (TARDEC), especially Dr. Paramsothy Jayakumar, for their feedback and suggestions. We would also like to thank TARDEC for the use of their HPC cluster computer, which was used to conduct the majority of the DEM simulations.

## References

- [1] M. G. Bekker, *Theory of land locomotion: the mechanics of vehicle mobility*. University of Michigan Press, 1956.
- [2] M. G. Bekker, *Off-the-road locomotion: research and development in terramechanics*. University of Michigan Press, 1960.
- [3] M. G. Bekker, *Introduction to terrain-vehicle systems*. Ann Arbor: University of Michigan Press, 1969.
- [4] R. A. Irani, R. J. Bauer, and A. Warkentin, "A dynamic terramechanic model for small lightweight vehicles with rigid wheels and grousers operating in sandy soil," *J. Terramechanics*, vol. 48, pp. 307–318, Aug. 2011.
- [5] Z. Jia, W. Smith, and H. Peng, "Fast analytical models of wheeled locomotion in deformable terrain for mobile robots," *Robotica*, pp. 1–19, Mar. 2012.
- [6] M. Sutoh, J. Yusa, T. Ito, K. Nagatani, and K. Yoshida, "Traveling performance evaluation of planetary rovers on loose soil," *J. Field Robot.*, 2012.
- [7] M. Sutoh, K. Nagaoka, K. Nagatani, and K. Yoshida, "Design of wheels with grousers for planetary rovers traveling over loose soil," *J. Terramechanics*, Jul. 2013.
- [8] K. Iagnemma, S. Kang, H. Shibly, and S. Dubowsky, "Online Terrain Parameter Estimation for Wheeled Mobile Robots With Application to Planetary Rovers," *IEEE Trans. Robot.*, vol. 20, pp. 921–927, Oct. 2004.
- [9] L. Ding, K. Yoshida, K. Nagatani, H. Gao, and Z. Deng, "Parameter identification for planetary soil based on a decoupled analytical wheel-soil interaction terramechanics model," 2009, pp. 4122–4127.
- [10] Z. Jia, W. Smith, and H. Peng, "Fast computation of wheel-soil interactions for safe and efficient operation of mobile robots," presented at the 2011 IEEE/RSJ International Conference on Intelligent Robots and Systems (IROS), 2011, pp. 3004–3010.
- [11] J. Wong and A. Reece, "Prediction of rigid wheel performance based on the analysis of soil-wheel stresses part I. Performance of driven rigid wheels," *J. Terramechanics*, vol. 4, pp. 81–98, 1967.
- [12] J. Wong and A. Reece, "Prediction of rigid wheel performance based on the analysis of soil-wheel stresses part II. Performance of towed rigid wheels," *J. Terramechanics*, vol. 4, pp. 7–25, 1967.
- [13] H. Shibly, K. Iagnemma, and S. Dubowsky, "An equivalent soil mechanics formulation for rigid wheels in deformable terrain, with application to planetary exploration rovers," *J. Terramechanics*, vol. 42, no. 1, pp. 1–13, Jan. 2005.
- [14] C. Senatore and C. Sandu, "Off-road tire modeling and the multi-pass effect for vehicle dynamics simulation," *J. Terramechanics*, vol. 48, pp. 265–276, Aug. 2011.
- [15] G. Meirion-Griffith and M. Spenko, "A pressure-sinkage model for small-diameter wheels on compactive, deformable terrain," *J. Terramechanics*, Jul. 2012.
- [16] B. Schäfer, A. Gibbesch, R. Krenn, and B. Rebele, "Planetary rover mobility simulation on soft and uneven terrain," *Veh. Syst. Dyn.*, vol. 48, no. 1, pp. 149–169, Jan. 2010.
- [17] B. Trease, R. Arvidson, R. Lindemann, K. Bennett, F. Zhou, K. Iagnemma, C. Senatore, and L. Van Dyke, "Dynamic modeling and soil mechanics for path planning of the Mars exploration rovers," in *IDETC/CIE*, Washington, D.C., 2011.
- [18] G. Ishigami, A. Miwa, K. Nagatani, and K. Yoshida, "Terramechanics-based model for steering maneuver

- of planetary exploration rovers on loose soil,” *J. Field Robot.*, vol. 24, no. 3, pp. 233–250, Mar. 2007.
- [19] Z. Jia, W. Smith, and H. Peng, “Terramechanics-based wheel–terrain interaction model and its applications to off-road wheeled mobile robots,” *Robotica*, pp. 1–13, Jul. 2011.
- [20] R. N. Yong and E. A. Fattah, “Prediction of wheel–soil interaction and performance using the finite element method,” *J. Terramechanics*, vol. 13, no. 4, pp. 227–240, Dec. 1976.
- [21] M. A. Knuth, J. B. Johnson, M. A. Hopkins, R. J. Sullivan, and J. M. Moore, “Discrete element modeling of a Mars Exploration Rover wheel in granular material,” *J. Terramechanics*, Oct. 2011.
- [22] T. Tsuji, Y. Nakagawa, N. Matsumoto, Y. Kadono, T. Takayama, and T. Tanaka, “3-D DEM simulation of cohesive soil–pushing behavior by bulldozer blade,” *J. Terramechanics*, vol. 49, no. 1, pp. 37–47, Feb. 2012.
- [23] C. Kloss and C. Goniva, “LIGGGHTS: A new open source discrete element simulation software,” in *5th International Conference on Discrete Element Methods*, London, UK, 2010.
- [24] K. Iwashita and M. Oda, “Rolling Resistance at Contacts in Simulation of Shear Band Development by DEM,” *J. Eng. Mech.*, vol. 124, no. 3, pp. 285–292, 1998.
- [25] K. L. Johnson, K. Kendall, and A. D. Roberts, “Surface Energy and the Contact of Elastic Solids,” *Proc. R. Soc. Math. Phys. Eng. Sci.*, vol. 324, no. 1558, pp. 301–313, Sep. 1971.
- [26] H. Zhang and H. Makse, “Jamming transition in emulsions and granular materials,” *Phys. Rev. E*, vol. 72, no. 1, Jul. 2005.
- [27] N. Brilliantov, F. Spahn, J.-M. Hertzsch, and T. Pöschel, “Model for collisions in granular gases,” *Phys. Rev. E*, vol. 53, no. 5, pp. 5382–5392, May 1996.
- [28] L. Silbert, D. Ertas, G. Grest, T. Halsey, D. Levine, and S. Plimpton, “Granular flow down an inclined plane: Bagnold scaling and rheology,” *Phys. Rev. E*, vol. 64, no. 5, Oct. 2001.
- [29] C. Salot, P. Gotteland, and P. Villard, “Influence of relative density on granular materials behavior: DEM simulations of triaxial tests,” *Granul. Matter*, vol. 11, no. 4, pp. 221–236, Apr. 2009.
- [30] T. Matsushima, J. Katagiri, K. Uesugi, A. Tsuchiyama, and T. Nakano, “3D Shape Characterization and Image-Based DEM Simulation of the Lunar Soil Simulant FJS-1,” *J. Aeronaut. Eng.*, vol. 22, no. 1, p. 15, 2009.
- [31] J.-P. Plassiard, N. Belheine, and F.-V. Donzé, “A spherical discrete element model: calibration procedure and incremental response,” *Granul. Matter*, vol. 11, no. 5, pp. 293–306, Mar. 2009.
- [32] A. P. Grima and P. W. Wypych, “Discrete element simulations of granular pile formation: Method for calibrating discrete element models,” *Eng. Comput.*, vol. 28, no. 3, pp. 314–339, 2011.
- [33] C. M. Wensrich and A. Katterfeld, “Rolling friction as a technique for modelling particle shape in DEM,” *Powder Technol.*, vol. 217, pp. 409–417, Feb. 2012.
- [34] J. Ai, J.-F. Chen, J. M. Rotter, and J. Y. Ooi, “Assessment of rolling resistance models in discrete element simulations,” *Powder Technol.*, vol. 206, no. 3, pp. 269–282, Jan. 2011.
- [35] B. Yeomans, C. M. Saaj, and M. Van Winnendael, “Walking planetary rovers – Experimental analysis and modelling of leg thrust in loose granular soils,” *J. Terramechanics*, vol. 50, no. 2, pp. 107–120, Apr. 2013.
- [36] G. H. Peters, W. Abbey, G. H. Bearman, G. S. Mungas, J. A. Smith, R. C. Anderson, S. Douglas, and L. W. Beegle, “Mojave Mars simulant—Characterization of a new geologic Mars analog,” *Icarus*, vol. 197, no. 2, pp. 470–479, Oct. 2008.
- [37] M. Apfelbeck, S. Kuß, B. Rebele, and B. Schäfer, “A systematic approach to reliably characterize soils based on Bevameter testing,” *J. Terramechanics*, vol. 48, pp. 360–371, Oct. 2011.
- [38] I. Shmulevich, “State of the art modeling of soil–tillage interaction using discrete element method,” *Soil Tillage Res.*, vol. 111, no. 1, pp. 41–53, Dec. 2010.
- [39] V. Vedachalam, “Discrete Element Modelling of Granular Snow Particles Using LIGGGHTS,” M.Sc., University of Edinburgh, 2011.
- [40] H. P. Zhu, Z. Y. Zhou, R. Y. Yang, and A. B. Yu, “Discrete particle simulation of particulate systems: A review of major applications and findings,” *Chem. Eng. Sci.*, vol. 63, no. 23, pp. 5728–5770, Dec. 2008.
- [41] R. Briand, P. Radziszewski, and D. Pasini, “Virtual soil calibration for wheel–soil interaction simulations using the discrete-element method,” *Can. Aeronaut. Space J.*, vol. 57, no. 1, pp. 59–64, Apr. 2011.
- [42] Y. Fu, “Experimental Quantification and DEM Simulation of Micro-Macro Behaviors of Granular Materials Using X-Ray Tomography Imaging,” Doctor of Philosophy, Department of Civil and Environmental Engineering, Louisiana State University and Agricultural and Mechanical College, 2005.
- [43] J. Liu, B. Yun, and C. Zhao, “Identification and Validation of Rolling Friction Models by Dynamic Simulation of Sandpile Formation,” *Int. J. Geomech.*, vol. 12, no. 4, pp. 484–493, Aug. 2012.
- [44] N. Belheine, J.-P. Plassiard, F.-V. Donzé, F. Darve, and A. Seridi, “Numerical simulation of drained triaxial test using 3D discrete element modeling,” *Comput. Geotech.*, vol. 36, no. 1–2, pp. 320–331, Jan. 2009.
- [45] C. Senatore, M. Wulfmeier, J. MacLennan, P. Jayakumar, and K. Iagnemma, “Investigation of stress and failure in granular soils for lightweight robotic vehicle applications,” in *Modeling &*

- Simulation, Testing and Validation (MSTV) Mini-Symposium*, Michigan, 2012.
- [46] J. Wong, *Terramechanics and off-road vehicle engineering: terrain behaviour, off-road vehicle performance and design*, 2nd ed. Amsterdam, The Netherlands: Butterworth-Heinemann, 2010.
- [47] C. Senatore and K. Iagnemma, "Direct shear behaviour of dry, granular soils for low normal stress with application to lightweight robotic vehicle modelling," in *Proceedings of the 17th ISTVS International Conference*, Blacksburg, Virginia, 2011.
- [48] L. Ding, H. Gao, Z. Deng, K. Nagatani, and K. Yoshida, "Experimental study and analysis on driving wheels' performance for planetary exploration rovers moving in deformable soil," *J. Terramechanics*, vol. 48, pp. 27–45, Feb. 2011.